Available online at www.sciencedirect.com

jmr&t Journal of Materials Research and Technology

journal homepage: www.elsevier.com/locate/jmrt

Original Article

Microstructure and mechanical properties of pseudo binary eutectic Al–Mg_2Si alloy processed by laser powder bed fusion

Feipeng Yang [a], *Jianying Wang* [a], *Tao Wen* [a], *Xinhai Ai* [a], *Xixi Dong* [b,**], *Hailin Yang* [a,*], *Shouxun Ji* [c]

[a] *State Key Laboratory of Powder Metallurgy, Central South University, Changsha, 410083, China*

[b] *College of Mechanical and Electrical Engineering, Nanjing University of Aeronautics and Astronautics, Nanjing, 210016, China*

[c] *Brunel Centre for Advanced Solidification Technology (BCAST), Brunel University London, Uxbridge, Middlesex, UB8 3PH, United Kingdom*

ARTICLE INFO

Article history:
Received 29 December 2022
Accepted 19 March 2023
Available online 23 March 2023

Keywords:
Aluminium alloys
Microstructure
Mechanical properties
Additive manufacturing
Laser powder bed fusion

ABSTRACT

The traditional wrought Al–Mg–Si alloys fabricated via laser powder bed fusion (LPBF) are prone to hot cracks, unless adding grain refiners in as-LPBFed Al alloys. In this work, the Al-9.6 wt.%Mg-4.9 wt.%Si (equivalent to pseudo binary eutectic Al-13.3 wt.%Mg_2Si) alloy with low solidification range and hot-cracking susceptibility was successfully processed by LPBF. The as-LPBFed alloys have reached a high relative density of 99.3% at the VED of 129.6 J/mm^3. The microstructures were featured by fine α-Al grains and cellular eutectic Mg_2Si, accompanied by a high number density of dislocations, coherent GP zone and α-$Al_{12}(Fe,Mn)_3Si$ phases. The as-LPBFed Al-13.3Mg_2Si alloy exhibited the high ultimate tensile strength of 557 MPa, yield strength of 439 MPa and elongation of 2.9%. In addition to the grain refinement and dislocation strengthening, the strength enhancement is mainly ascribed to the dispersion strengthening from the divorced nanosized eutectic Mg_2Si. The results demonstrate that manipulation of alloys at near eutectic composition is effective to achieve high strength Al–Mg–Si alloys processed by LPBF.

1. Introduction

Additive manufacturing (AM) is becoming an important manufacturing method due to the unique advantages in design complicity, structural flexibility, customized products and improved mechanical performance [1]. Laser powder bed fusion (LPBF) is one of the popular AM technologies, capable of processing metallic materials including steels [2], Ti-alloys [3], Cu-alloys [4], Al alloys [5] and others. However, when applying LPBF to Al alloys, defects such as porosity and hot cracking are often formed due to the high thermal conductivity, high laser

* Corresponding author.
** Corresponding author.
E-mail addresses: dongxixi@nuaa.edu.cn (X. Dong), y-hailin@csu.edu.cn (H. Yang).

https://doi.org/10.1016/j.jmrt.2023.03.147

reflectivity and easy oxidization of Al powders [6,7]. Currently, it is more problematic in traditional wrought Al alloys than cast Al alloys for LPBF processing because of differences in solidification behaviours and hot-cracking susceptibility [7]. Therefore, continuous efforts are undertaking to develop high strength and crack-free Al alloys to be suitable for LPBF.

Approaches have been found to be effective in designing high strength as-LPBFed Al alloys. The first technical approach is to modify existing Al alloys with grain refiners. For example, Sc and Zr elements were used to promote the equiaxed α-Al grains, which could accommodate the stress and hot cracks during solidification in LPBF [5]. The Zr/Sc-modified crack free as-LPBFed Al–Cu [8], Al–Mg–Si [9] and Al–Zn–Mg–Cu [10] alloys have been reported, which exhibited a promisingly high ultimate tensile strength (UTS) of 441–487.3 MPa with elongation (El) of 14.1–17.7%. Also, the inoculation of Al alloys with nanoparticles was also found to be effective for eliminating hot cracking and promoting the transition between columnar to equiaxed grains, leading to the enhancement of LPBF processability [11–14]. Typically, for wrought Al–Mg–Si alloys, the processability of LPBF can be effectively improved by modifying alloy compositions. Li et al. [15] found that addition of the Sc/Zr elements could significantly increase the strength and decrease hot-cracking susceptibility in as-LPBFed Al-8.0Mg-1.3Si alloy, in which the UTS of 497 MPa and El of 11% have been achieved. Similarly, the Zr/Sc-modified Al-14.1Mg-0.47Si alloy processed by LPBF have exhibited the high density of 99.4% and high UTS of 510 MPa [16]. Moreover, it is reported that the Zr-modified 6061 (Al-1.14Mg-0.78Si) alloy was capable of processing by LPBF to obtain crack free components [17], the UTS and El reached 268 MPa and 26.5%, respectively. Also, the addition of nano-sized particles, such as YSZ [12], ZrO_2 and Y_2O_3 [18] could fully avoid the formation of hot cracking in as-LPBFed 6061 alloy. The increased nucleation sites for α-Al phase were enhanced by *ex-situ* nanoparticles, promoting the columnar-to-equiaxed transition [18]. It is noted that fine equiaxed grains with more boundaries suppressed the propagations of hot cracking [5].

Another technical approach is to develop novel alloys. The new Al-Cu [19], Al-Si [20,21], Al-Mg [22] and Al–Zn–Mg–Cu [23,24] based alloys have been developed for LPBF. It is found that the increase of solute contents (such as Mg, Si elements) in some extents can significantly reduce defects. This is due to the formation of eutectic phases with low melt point (e.g. α-Al/Si and α-Al/Mg_2Si phases), which promote the melt feeding during solidification [19–24]. Therefore, it is a natural consideration that the trials for eutectic alloys should be promising, because of their narrow solidification range from liquidus to solidus temperatures, low hot cracking tendency and the potential for solution strengthening. For instance, the cast Al–Si alloys with near eutectic compositions such as Al–10Si [25] and Al–12Si [26] have been popular in LPBF. Recently, the newly designed near eutectic Al–Fe [27], Al–Ce [28] and Al–Ni [29] alloys were developed. These Al alloys exhibited a full dense surface and superior mechanical properties at elevated temperatures. Also, the combination of utilizing eutectic alloys and the inoculation effect was confirmed as an effective strategy in designing high strength as-LPBFed Al alloys. For example, the Zr-modified near eutectic Al–Fe alloys were designed for LPBF, which showed a high yield strength (YS) of 500 MPa and high density of 99.7% [30]. Further, the microstructural heterogeneity in as-LPBFed Al–Fe–Zr alloys was manipulated via composition optimization of Zr content, exhibiting high strength and toughness simultaneously [31]. However, few studies have been reported for as-LPBFed Al–Mg–Si alloys with a composition near eutectic point, although it is believed that the systems with narrow solidification range can be significantly beneficial to the reduction of hot cracking in LPBF process.

Al–Mg_2Si pseudo binary eutectic alloy system, with the weight ratio of Mg/Si = 1.73, is a typical Al–Mg–Si based alloy. In this context, Al–Mg_2Si alloys are among the precipitation-hardening alloys with the strengthening Mg_2Si phase. The Mg_2Si showed low density (1.99×10^3 kgm^{-3}), low coefficient of thermal expansion (7.5×10^{-6} K^{-1}), high melting temperature (1085 °C), high hardness (4.5×10^9 Nm^{-2}) and high elastic modulus (120 GPa) [32]. In addition to the dendritic primary Mg_2Si, the α-Al/Mg_2Si eutectics were also formed in as-cast Al–Mg_2Si alloys, which were featured by the lamella, rod and flake structures [33]. It is found the as-cast Al–Mg_2Si alloys showed the UTS of 245–350 MPa with the El of 1.5–16.9% [34,35]. Furthermore, the microalloying of the Al–Mg_2Si alloys produced strengthening response with the UTS of 360–430 MPa and El of 3.5–8.6%, due to the formation of fine precipitated phases after heat treatment [35]. Based on previous success in as-cast Al–Mg_2Si alloys, it is attractive to investigate Al–Mg_2Si pseudo binary eutectic alloy system using LPBF because of its unique advantages, including the low cost of raw materials, excellent castability and potential of precipitation strengthening.

The present study aims to design a near eutectic Al-9.6Mg-4.9Si (pseudo binary eutectic Al-13.3Mg_2Si) alloy for LPBF. The processability, microstructure and mechanical properties of the alloy were systematically assessed under as-LPBFed condition. Discussion focuses on the fundamentals for lowering hot-cracking susceptibility of pseudo binary eutectic Al-13.3Mg_2Si alloy and the contribution of individual strengthening mechanisms to the as-LPBFed 13.3Mg_2Si alloy.

2. Experimental procedures

2.1. *Materials and LPBF process*

The cast ingot of Al-9.6Mg-4.9Si (wt.%) alloy was melted and atomized to powders under Ar atmosphere (Fig. 1a), with a particle size of 10.4 ~ 76.4 μm (Fig. 1b). The chemical composition of alloy powders was detected by inductively coupled plasma atomic emission spectrometry (ICP-AES, iCAP7600, USA), and the result is presented in Table 1. The as-LPBFed parts were fabricated using a metal 3D printing system, which contained the ytterbium fibre laser (IPG YLR-500-WC, Germany) and scanning galvanometers (Scanlab Hurryscan-20, Germany). The LPBF operation was performed under the Ar gas protection to avoid oxygen contamination [15]. The selected processing parameters are presented in Table 2, referring to our previous studies [36]. The schematic of LPBF process and the scanning strategy are presented in Figs. 2a

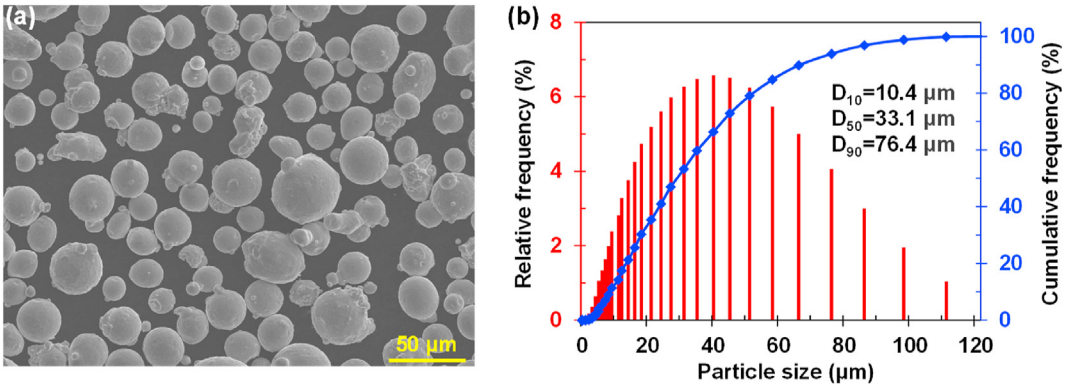

Fig. 1 – (a) SEM micrograph showing the morphology of the Al–Mg–Si alloy powder, (b) the distribution of particle size.

and b. The laser beam was scanned with a rotated 67° between the neighbouring layers (Fig. 2b).

2.2. *Characterization of as-LPBFed samples*

The relative density of the as-LPBFed samples were measured by Archimedes principle. The surface quality of samples was characterized by optical microscope (OM, Leica DM4000M, Germany). Phase constituent of the samples were detected via X-ray diffraction analysis (XRD, Rigaku; Japan) equipped with Cu *Ka* radiation. The typical microstructures were performed using scanning election microscope-backscattered electrons (SEM-BSE, FEI Nova Nano230, Netherlands). The inversed pole figure (IPF) was tested by electron backscattered diffraction (EBSD, FEI Nova Nano230, Netherlands). Based on the results of EBSD, the mean grain size was obtained from the TSL OIM Analysis software. The samples for EBSD analysis were prepared by electropolishing (immersed in methanol-nitric acid solution for 10 s at 15 V). The cellular structures and phase identification were conducted via transmission electron microscope (TEM, Talos F200X, Czech Republic). The TEM samples were polished using the ion polishing system (PIPS, Gatan 691, American). The material testing system (MTS, Alliance RT/30) was used to evaluate the tensile properties, operated with a strain rate of 1×10^{-3} s^{-1}. And the standard as-LPBFed samples for tensile tests were shown Fig. 2c, with a dimension of 80 mm × 10 mm × 2 mm (Fig. 2d). The loading direction of tensile testing was perpendicular to the LPBF building direction.

Table 1 – The composition of experimental alloy powder measured by ICP-AES (wt.%).

Alloy	Mg	Si	Mn	Fe	Al
Al–Mg–Si	9.62	4.88	0.74	0.21	Balance

3. Results

3.1. *The phase diagram of Al–Mg_2Si pseudo binary eutectic alloy*

The equilibrium phase diagram of Al–Mg–Si alloy calculated by Pandat is presented as Al–Mg_2Si pseudo-binary system in Fig. 3. It is shown that the pseudo-binary system has a eutectic point at 13.9 wt.% Mg_2Si. In this study, the Al-9.6Mg-4.9Si alloy can be expressed as Al-13.3Mg_2Si alloy in the pseudo-binary system, which is very close to the eutectic point. At the content of 13.3 wt.% Mg_2Si in equilibrium phase diagram, the solidification range is from 593.5 °C to 578.2 °C. The alloy was composed of primary α-Al phase and eutectic Mg_2Si phase. Compared with the solidification range of traditional wrought Al alloys [7], the near eutectic Al-13.3Mg_2Si alloy exhibited a narrow solidification range only 15.3 °C. Therefore, it is believed that the lower hot-cracking susceptibility of as-LPBFed near eutectic Al-13.3Mg_2Si alloy would be achieved due to its narrow solidification range.

3.2. *Process optimization for LPBF*

The process parameters, including laser powder (P), scan speed (*v*), hatch spacing (*t*) and layer thickness (*h*), are associated with the volumetric energy density (*VED*), which can be shown as [37]: $VED=P/vht$. The relationship between the *VED* and relative density is shown in Fig. 4. The dense (~99.3%) Al-13.3Mg_2Si alloy was obtained with the optimized *VED* (i.e. *VED* = 129.6 J/mm^3, where laser powder was 350 W, scan speed was 900 mm/s). Typically, three optical images of as-LPBFed alloys are shown in Fig. 4b–d, which were fabricated at 75 J/mm^3, 129.6 J/mm^3 and 150 J/mm^3, respectively. At a lower *VED* of 75 J/mm^3, the crescent shaped defects were detected in Fig. 4b, the un-melted alloy powders were observed in the as-LPBFed sample. With increased *VEDs*, the liquid phase of powder

Table 2 – The processing parameters of as-LPBFed samples.

Laser powder (W)	Scan speed (mm/s)	Hatch spacing (mm)	Layer thickness (mm)	Preheat temperature (°C)
270/310/350	600/900/120	0.1	0.03	100

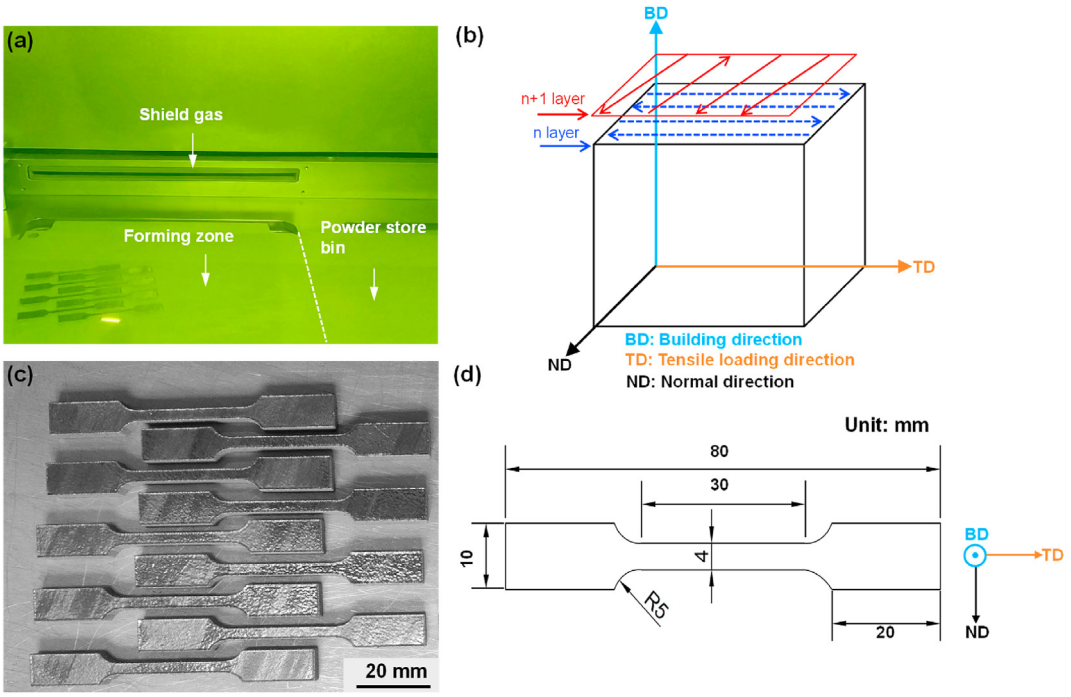

Fig. 2 – (a) LPBF processing of the Al–Mg–Si alloy, (b) laser beam scanning strategy during sample fabrication, (c) optical micrograph showing the tensile samples, and (d) the dimension of tensile test samples.

was formed and fully diffused in the melt pool. Thus, the density was increased to the maximum when *VED* was 129.6 J/mm^3, as shown in Fig. 4c. However, the limited gas pores still appeared in the as-LPBFed samples. When the *VED* exceeded 129.6 J/mm^3 (i.e. 150 J/mm^3), the circular keyholes were generated, as shown in Fig. 4d. The defect was occurred due to the evaporation of low melting point of elements during the LPBF processing. To verify the capability of manufacturing complex components with the Al-13.3Mg_2Si alloy further, the typical part manufactured at *VED* of 129.6 J/mm^3 is shown in Fig. 4e. The part without obvious macroscopic defects showed smooth and bright surface. Therefore, the microstructures were analysed using the samples processed by the *VED* of 129.6 J/mm^3.

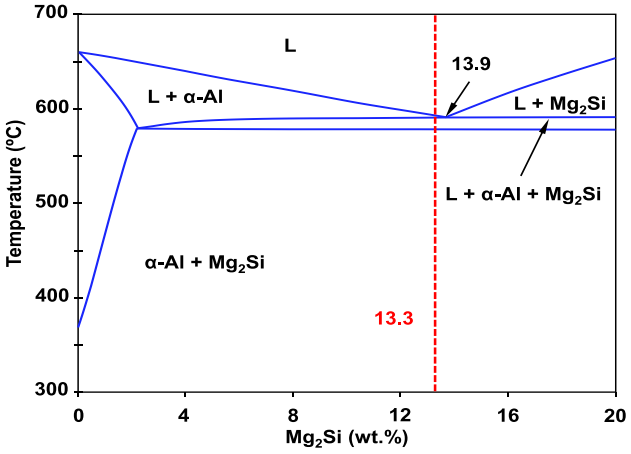

Fig. 3 – The equilibrium phase diagram of pseudo-binary Al–Mg_2Si alloy calculated by Pandat.

3.3. *Phase identification*

The XRD spectra of pre-alloyed powder and as-LPBFed alloy are shown in Fig. 5a. The diffraction peaks of α-Al and Mg_2Si phases were clearly visible, while the Mn/Fe-rich phase could not be detected because the Fe and Mn contents were below the detection limit. Compared with the diffraction peaks of powder, the α-Al peaks of as-LPBFed sample were slightly shifted to a higher angle (between 38° and 39° in Fig. 5b). This is likely due to the nonequilibrium solidification occurred during the LPBF process. Larger thermal stresses accumulated and more solute atoms dissolved into the gap of α-Al, leading to the distortion of α-Al crystal lattice [16].

3.4. *Microstructural characterization*

Fig. 6a shows the melt pool (MP) of as-LPBFed Al-13.3 Mg_2Si alloy along the building direction. The IPF maps in Fig. 6b indicated that the coarse columnar grains and fine equiaxed grains were found inside and near the melt pool boundaries (MPBs), respectively. This is consistent with the results of other as-LPBFed Al alloys [15,38]. Meanwhile, the average grain size in the as-LPBFed alloy was 18.6 μm on building section (Fig. 6c), which was significantly finer than that in conventional cast Al–Mg–Si alloys (94 ~ 108 μm) [39,40]. The grain boundary orientation angle distribution on building direction is shown in Fig. 6d, the proportion of low angle grain boundaries (LAGBs, <15°) was measured to be 68.2% in the as-LPBFed alloy. The LAGBs might play a role in facilitating the

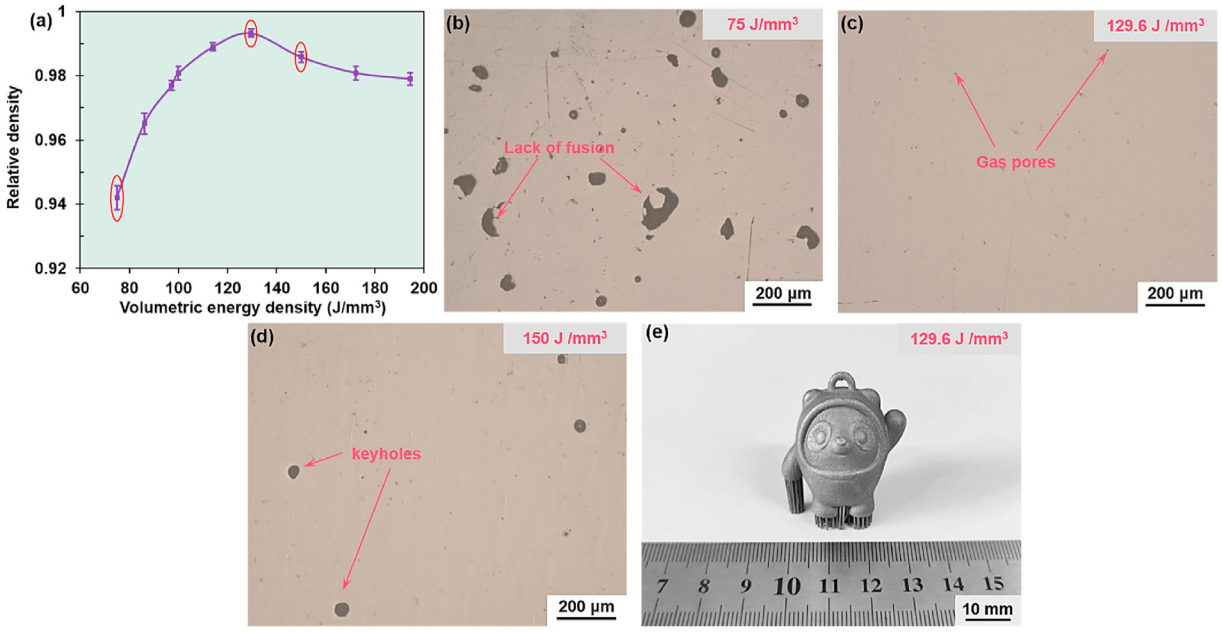

Fig. 4 – (a) The relative density of as-LPBFed Al-13.3Mg_2Si alloy fabricated at different *VEDs*, optical micrographs of the as-LPBFed alloys obtained at (b) 75 J/mm^3, (c) 129.6 J/mm^3 (d) 150 J/mm^3, and (e) the complex component made at *VED* of 129.6 J/mm^3.

local nucleation and the growth of precipitated phases [41], resulting in the enhancement in strength. In Fig. 7a, the typical microstructures near the MPB were divided into three zones, including the coarse zone (Fig. 7b), fine zone (Fig. 7c) and heat affected zone (HAZ) (Fig. 7d). The elongated and cellular eutectic microstructures were observed in the coarse and fine zones respectively, which was closely related with the formation of Mg_2Si phases during eutectic solidification. The eutectic structures were featured by grey α-Al and black eutectic Mg_2Si phases. However, the Mg_2Si network was broken inside the HAZ, showing irregular particles. This can be attributed to the effect of continuous thermal cycling around the MPBs. The variation of microstructures was associated with the temperature gradient and growth rate, which were resulted from the rapid solidification during LPBF [38].

Furthermore, TEM images along the [011] Al zones axis (Fig. 8) revealed the microstructures of as-LPBFed Al-13.3Mg_2Si alloy. Obviously, a large number of cellular structures were uniformly distributed in Fig. 8a. The microstructural characteristics of the cellular structures are consistent with the fine zone of MP (Fig. 7c). High angle annular dark field (HAADF) STEM image is presented in Fig. 8b for the cellular structures and the detailed elements distribution is shown in Fig. 8c. It is seen that Mg and Si distributed uniformly inside the α-Al phase but visible variation along the cellular boundaries, verifying that the α-Al/Mg_2Si eutectics were divorced. The extremely fast cooling rate during the non-equilibrium solidification process produces a highly segregated zone near the boundaries of α-Al and Mg_2Si phases, which is typical for a completely divorced eutectic [42]. As a result, the phases in

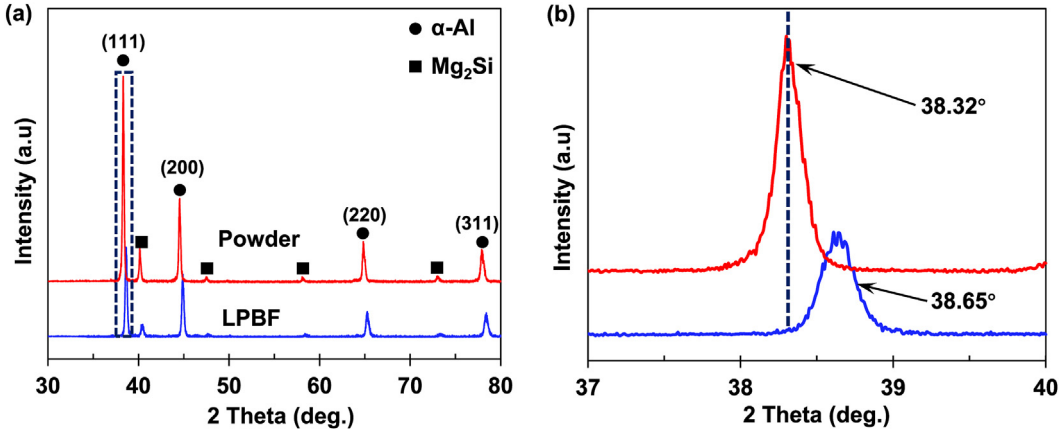

Fig. 5 – (a) XRD spectra for phase analysis in the powder and as-LPBFed Al-13.3Mg_2Si alloy, (b) detailed spectra from 37° to 40° in the as-LPBFed Al-13.3Mg_2Si alloy.

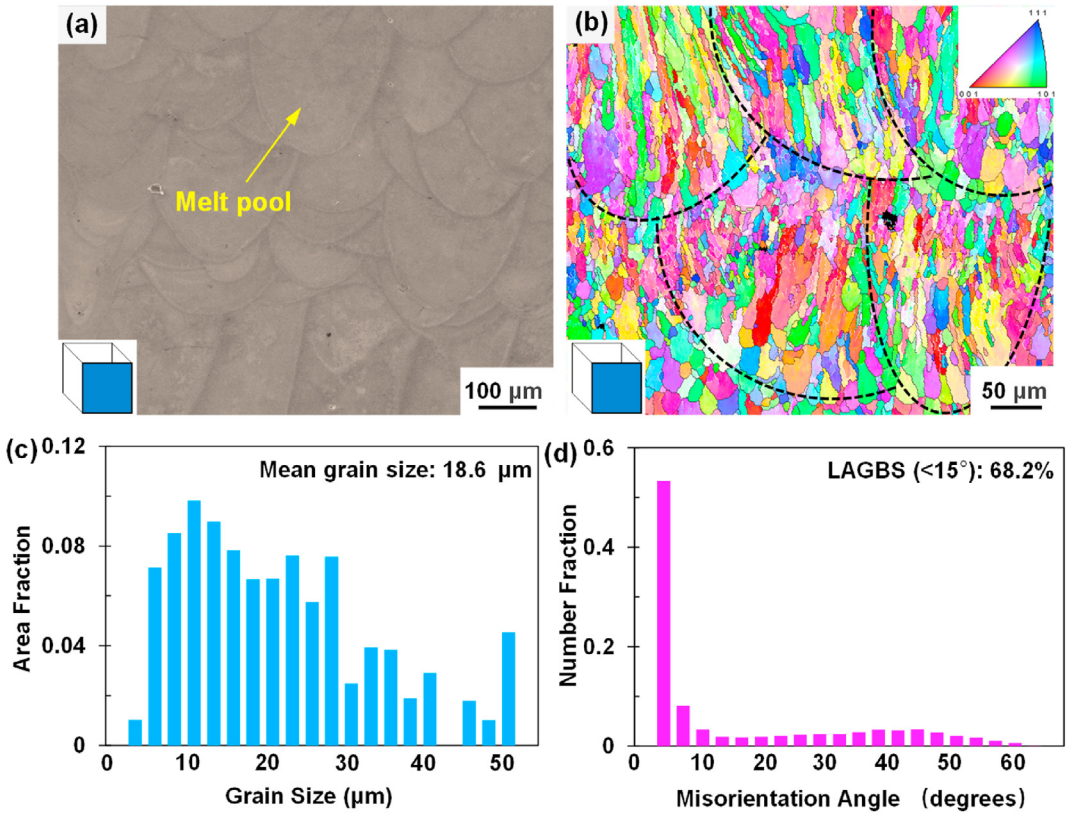

Fig. 6 – (a) SEM image showing the melt pools, (b) the inversed pole figure (IPF) images along the building direction, (c) the grain size distribution and (d) grain boundary orientation angle distribution along building direction of the as-LPBFed Al-13.3Mg_2Si alloy.

divorced eutectics grow independently but in a successive manner [43]. Also, it is observed that most of Mn and Fe elements could be observed in the vicinity of Mg_2Si phase, and the Mn/Fe-rich phase consisted of Al, Fe, Mn and Si elements.

Meanwhile, a high number density of dislocations were also observed in as-LPBFed samples (Fig. 9a). In Fig. 9b, fine nanoprecipitates were observed in the cellular structure. Particularly, three regions containing different nanoprecipitates were marked by the rectangles. In Fig. 9c, the high-resolution TEM (HR-TEM) image showed the limited needle-shaped nanoprecipitates existing inside the cell. And the fast Fourier transform (FFT) image (Fig. 9d) presented the distinct straight streaks, indicating that the needle-shaped precipitates inside the cell was GP zone. The formation of limited GP zones probably resulted from the intrinsic thermal effects during LPBF process. Moreover, the limited GP zone showed coherent interface with the α-Al matrix. The HR-TEM image of eutectic Mg_2Si nanoparticles is displayed in Fig. 9e. It can be seen that Mg_2Si particles showed a very good lattice matching with α-Al phase (Fig. 9f). According to the measured lattice parameters, the interplanar spacing of α-Al and Mg_2Si were 2.35 Å and 2.28 Å, respectively, which were identified as the planes of $(\bar{1}11)_{\alpha\text{-Al}}$ and $(\bar{2}20)_{Mg2Si}$. Therefore, the orientation relationship between α-Al and Mg_2Si was expressed as $(\bar{2}00)_{\alpha\text{-Al}}$// $(200)_{Mg2Si}$, $(\bar{1}\bar{1}1)_{Al}$// $(220)_{Mg2Si}$ and $[011]_{Al}$//$[001]_{Mg2Si}$. Similarly, the corresponding HRTEM and FFT images of Mn/Fe-rich phase are shown in Figs. 9g and h, implying the semi-coherent relationship between the α-Al and α-$Al_{12}(Fe,Mn)_3Si$. It can be expressed as $(1\bar{1}1)_{Al}$//$(420)_{\alpha\text{-Al12(Fe,Mn)3Si}}$, $(\bar{1}1\bar{1})_{Al}$//$(0\bar{2}2)_{\alpha\text{-Al12(Fe,Mn)3Si}}$ and $[011]_{Al}$// $[\bar{1}22]_{\alpha\text{-Al12(Fe,Mn)3Si}}$. The interplanar spacing of α-Al and α-$Al_{12}(Fe,Mn)_3Si$ were 2.35 Å for $(\bar{1}11)$ and 9.25 Å for $(0\bar{2}2)$, respectively. The interaction between nanoprecipitates and dislocations could be likely promoted due to the well-developed interfaces between nanoprecipitates and α-Al matrix, simultaneously resulting in Orowan strengthening in the Al alloys [36].

3.5. *Mechanical properties*

The tensile properties of as-LPBFed Al-13.3Mg_2Si samples are shown in Fig. 10a. The as-LPBFed alloys have achieved significant improvement in mechanical properties with the UTS of 557 ± 6 MPa, YS of 439 ± 4 MPa and El of 2.9 ± 0.2%. The detailed comparisons of mechanical properties between the as-LPBFed Al-13.3Mg_2Si alloy with reported Al alloys under different processing conditions are summarized in Fig. 10b. It is noted that the strength of as-LPBFed Al-13.3Mg_2Si alloys is significantly enhanced compared with as-cast parts [34,35], which is mainly due to the refined microstructures resulted from high cooling rates. The cooling rates are normally less than 10^2 K/s in casting process [44], leading to the formation of micro-scaled Mg_2Si phases [35]. In contrast, the higher cooling rates (10^6–10^7 K/s) existed in LPBF process [45]. As a result, the

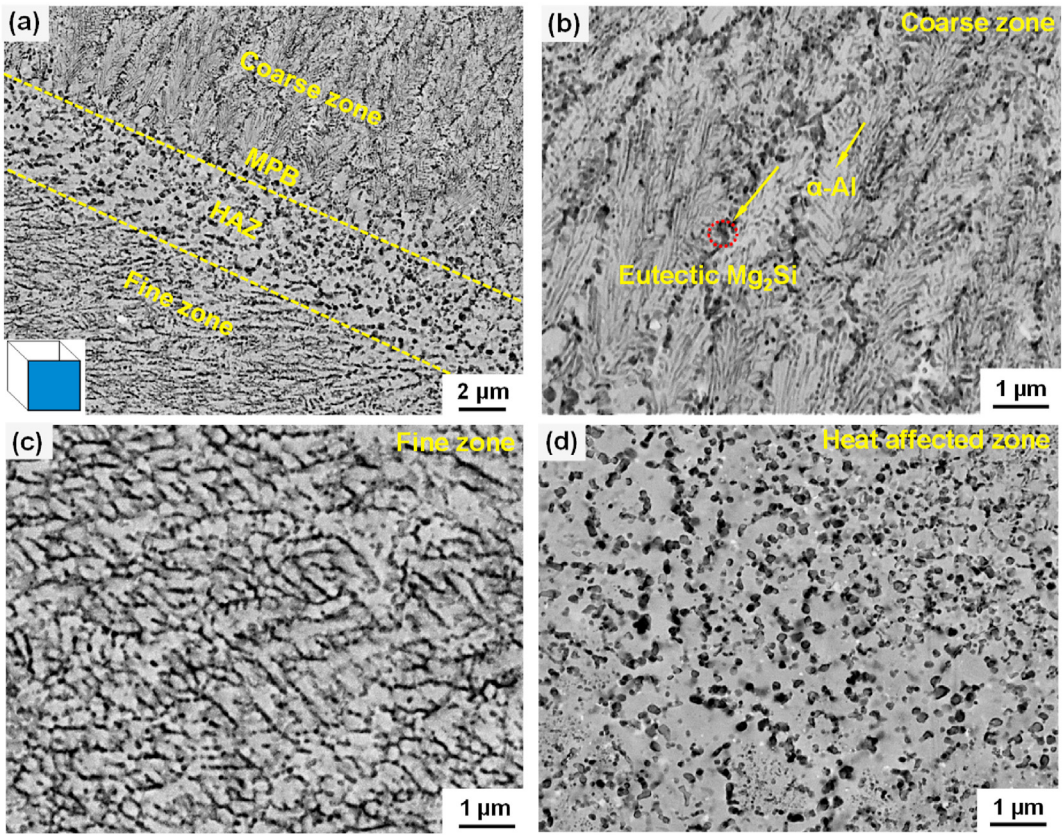

Fig. 7 – SEM/BSE images showing (a) the overall microstructure, (b) coarse zone, (c) fine zone and (d) heat affected zone around melt pool boundaries of the as-LPBFed Al-13.3Mg_2Si alloy.

refined Mg_2Si eutectics (~79 nm) were obtained to strengthen the as-LPBFed Al-13.3Mg_2Si alloys. Moreover, the as-LPBFed Al-13.3Mg_2Si alloy also exhibited superior strength compared with Al-Si [25,46–53], Zr modified AA6061 alloys [17,54] and even some costly Sc and Zr modified Al–Mg–Si alloys under LPBF fabrication [15,16]. However, the elongation is relatively inferior, which is associated with the pores and Mg_2Si eutectic in the as-LPBFed samples. It is verified that excessive Mg_2Si acted as brittle phase has adverse effect on the plasticity of Al alloys [55]. Similar phenomena have been found in as-LPBFed Al alloys containing excessive brittle Si [21].

The fractured surface of as-LPBFed samples is shown in Fig. 11a. Porosities with a diameter of 20–46 μm were seen in the fractured surface. Because these porosities could act as

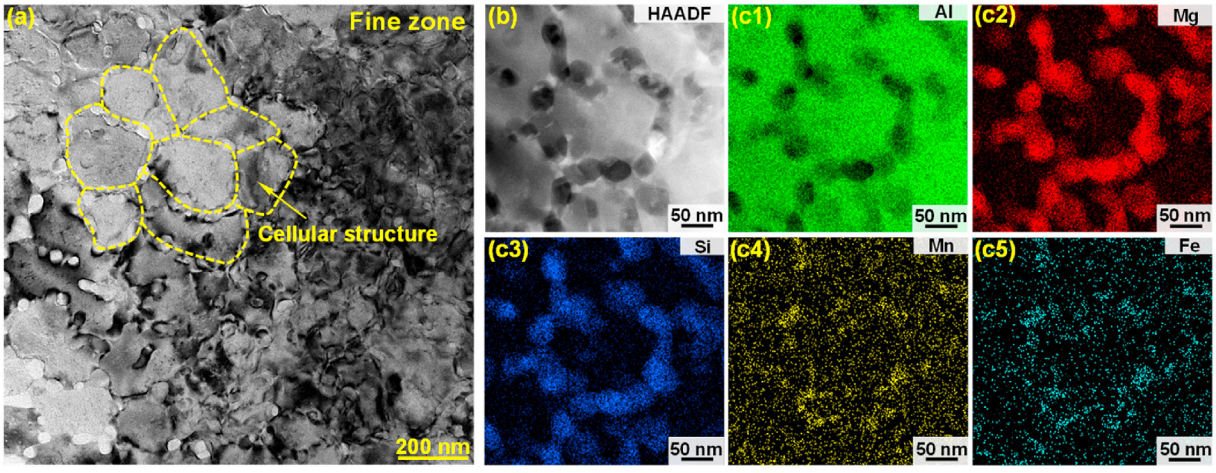

Fig. 8 – (a) TEM bright-field image showing the uniform cellular structures in fine zone, (b) HAADF-STEM image showing the cellular structures and (c) corresponding mapping of main elements including Al, Mg, Si, Mn and Fe.

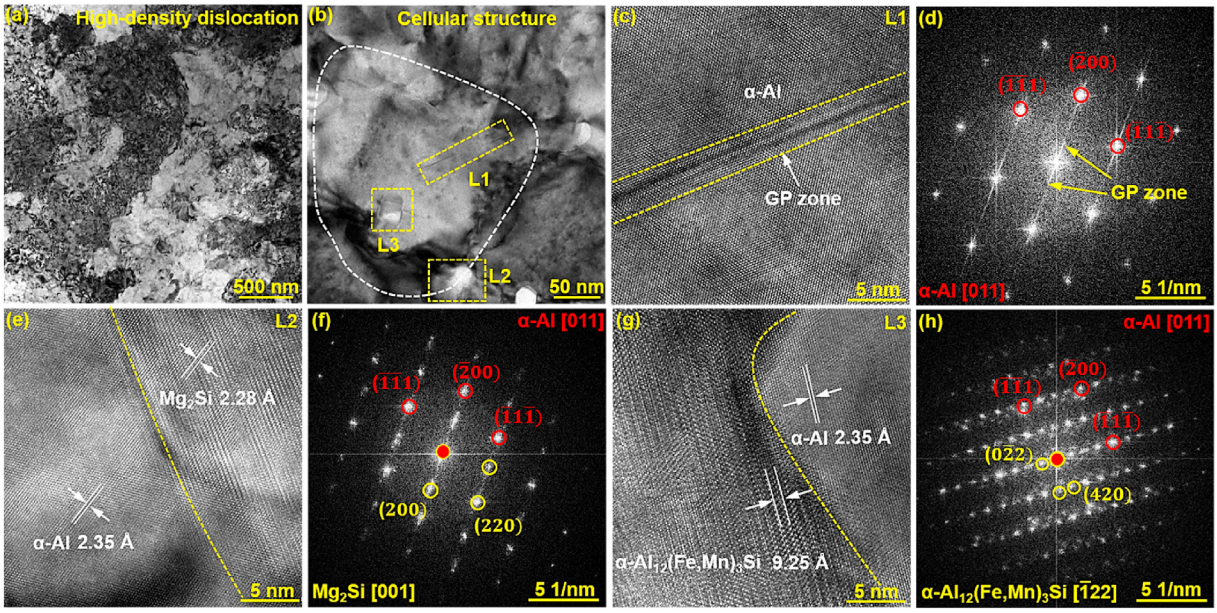

Fig. 9 – TEM bright-field images showing (a) a high number density of dislocations in the as-LPBFed sample, (b) the precipitates marked by rectangular with L1, L2, and L3 around the cellular eutectic structure, (c, e and g) high-resolution TEM images and (d, f and h) corresponding FFT patterns of the precipitates marked in (b), taken along the [011] zone axis.

stress concentration and crack initiation sites, thus tensile strength could be lowered than the data being expected. Typically, the large-scale cleavage steps were observed at the fractured surface (Fig. 11b). In Fig. 11c, the high magnification image showed very small and shallow dimples, indicating the ductile fractures existed there. Therefore, the as-LPBFed Al-13.3Mg_2Si alloy exhibited the combination of ductile-brittle fractures.

4. Discussion

4.1. *The processability of as-LPBFed Al-13.3Mg_2Si alloy*

4.1.1. *The effect of printing parameters on processability*

Generally, the as-LPBFed Al alloys are easier to form cracks, because of the high thermal conductivity, high laser reflectivity and easy oxidization of powder. In this work, the high relative density (99.3%) was achieved for the pseudo binary eutectic Al-13.3Mg_2Si alloy. Two strategies were adopted to obtain the dense and crack free alloy. Firstly, the process parameters were optimised to supply adequate heat energy for LPBF process. It is found that the high reflectivity (~91%) of Al powder decreased to a relatively low level 60%, when the temperature increased close to the melting point [56]. Meanwhile, a higher energy density is required during LPBF process, due to the rapid loss of heat from the high thermal conductivity of Al [57]. Therefore, the different *VEDs*, from 75 J/mm^3 to 194.4 J/mm^3, were explored to provide the appropriate temperatures required for LPBF process. Secondly, the rapid heating/cooling of LPBF processing is responsible for the volumetric thermal expansion/contraction, resulting in the generation of thermal stress within the as-LPBFed samples [58]. As the accumulation of thermal stress

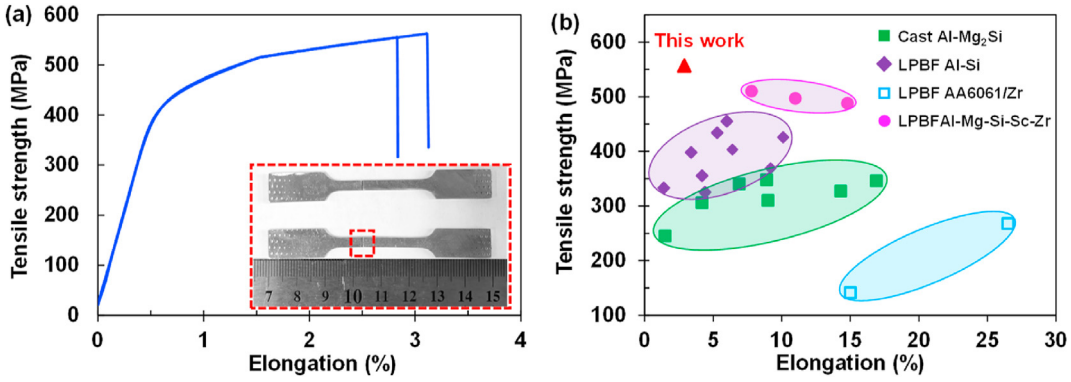

Fig. 10 – (a) Tensile stress–strain curves of as-LPBFed Al-13.3Mg_2Si alloys, the insert in (a) showing the sample after tensile test, (b) a comparison of the mechanical properties between the as-LPBFed Al-13.3Mg_2Si alloys and other Al alloys manufactured under different conditions.

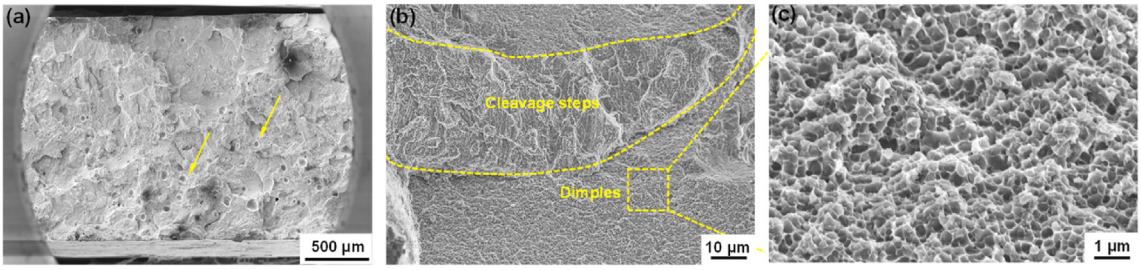

Fig. 11 – (a) The overall fractured morphology of as-LPBFed samples, (b) the typical fracture of as-LPBFed sample and (c) the magnified image of local region marked by yellow square frame in (b).

generated from the rapid solidification, the risk of forming cracks became noticeable. In this work, the pre-heating temperature was selected at 100 °C to eliminate the thermal stress during processing. Previous study has also demonstrated that stress accumulation could be effectively reduced by pre-heating the substrate during LPBF processing [59].

4.1.2. *The effect of eutectic Al–Mg_2Si phase on processability*

Meanwhile, the hot-cracking in as-LPBFed Al alloys have been attributed to specific characteristics of alloys, such as large differences between solidus and liquidus temperatures, the high coefficient of thermal expansion (CTE), and poor liquidus fluidity of the molten phase [7]. However, these three detrimental factors are improved effectively in this work. Firstly, based on the Kou's model [60], a larger temperature difference between the liquidus and solidification temperature tends to form higher hot cracking tendency. The wrought Al alloys have larger solidification range (i.e. 6061 alloy ~105 °C [17], 7075 alloy ~140 °C [61]) than cast Al–Si alloys [5], resulting in the high hot-cracking susceptibility of wrought Al alloys. In this study, a narrow solidification range (15.3 °C) of the Al-13.3Mg_2Si alloy was achieved via designing eutectic composition, which is considered as the predominant factor contributed to the low hot-cracking susceptibility [5]. Secondly, as shown in Fig. 3, the melting point of eutectic Al–Mg_2Si phase is only 572 °C. This suggests that the Al–Mg_2Si phases are adequately melted under the high temperature of LPBF process [14], leading to a better fluidity. Thus, the high fraction of eutectic in Al-13.3Mg_2Si alloy may help to backfill the hot cracking during the last stage of solidification. Thirdly, based on the Kingery's theory [62], the thermal stress is positively correlated with the CTE of material. It is noted that the CTE of Mg_2Si (7.5×10^{-6} K^{-1} [36]) is significantly lower than that of pure Al (22.6×10^{-6} K^{-1} [63]). The high Mg_2Si content tend to decrease the CTE of Al alloy, which also have potentials to decrease thermal stress and hot-cracking susceptibility in as-LPBFed Al-13.3Mg_2Si alloy.

4.2. *Strengthening in the as-LPBFed Al-13.3Mg_2Si alloy*

The considerable enhancement could be ascribed to fine grains, eutectic Mg_2Si, limited GP zone and α-$Al_{13}(Fe,Mn)_2Si$ nanoparticles, solid solution and high number density of dislocations in the as-LPBFed Al-13.3Mg_2Si alloy. The synergistic strengthening mechanisms include solid solution strengthening (σ_{ss}), dislocation strengthening (σ_{dis}), grain boundary strengthening (σ_{gb}), and dispersion strengthening (σ_{dps}). Correspondingly, the contribution to the total yield strength from the individual strengthening mechanism can be calculated and the results are presented in Table 3. The expression for the YS (σ_y) of as-LPBFed Al-13.3Mg_2Si alloy can be shown as:

$$\sigma_y = \sigma_{SS} + \sigma_{gb} + \sigma_{dis} + \sigma_{dps} \quad (1)$$

4.2.1. *Solid solution strengthening*

The solute solution strengthening from excess Mg (~1.1 wt%) should be taken into account. Note that the strengthening effect from Si phase is not involved in this study, due to the limited solid solubility of Si phase in Al matrix. Thus, yield strength is related to the solid solution effect by [64]:

$$\sigma_{SS} = \sum_i k_i c_i^{2/3}, (i = Mg) \quad (2)$$

where c_i is the concentration of *I* solute (in wt.%) and k_i is a scaling factor for the *i* solute: $k_{Mg} \approx 29.0$ MPa $(wt.\%)^{-2/3}$ [65]. The strength from Mg (~1.1wt%) is calculated to be 30.9 MPa.

4.2.2. *Dislocations strengthening*

As shown in Fig. 9a, the high dislocation of density is usually generated in as-LPBFed alloy, due to the high cooling rate during rapid solidification. The strengthening effect of high levels dislocations generated during LPBF process can be described by the Bailey-Hirsch formula [66]:

$$\sigma_{dis} = M\alpha G b \rho^{1/2} \quad (3)$$

where α is a constant with a value of 0.24, *M* is Taylor factor, *b* is Burger vector, *υ* is the Poisson's ratio, *G* is the shear modulus of the α-Al matrix, *ρ* is the dislocation density. The dislocation density was estimated based on the XRD results through the Williamson-Hall method, which describes that the broadening of the diffraction peak (β) including two parts, namely the crystallite size broadening (β_G) and the strain broadening

Table 3 – The contribution of the individual calculated to the total yield strength of the as-LPBFed Al-13.3Mg_2Si alloy.

σ_{SS}/MPa	σ_{dis}/MPa	σ_{gb}/MPa	σ_{dp}/MPa	Total σ/MPa
30.9	63.1	59.4	252	405

*A precision of 3 significant digits.

(β_S). Based on the assumption of a Cauchy-type function, the expression for β is given as [66]:

$$\beta = \beta_G + \beta_S \tag{4}$$

$$\beta_G = K\lambda / (D \cdot \cos\theta) \tag{5}$$

$$\beta_S = 4\varepsilon \cdot \tan\theta \tag{6}$$

where $K = 0.9$ is a constant, $\lambda = 0.15405$ nm is the wavelength of Cu-Kα radiation, D is the crystallite size, ε is the micro strain, and θ is the Bragg angle of the specific diffraction peak. Consequently, Eq. (4) can be simplified as:

$$\beta \cos\theta = K\lambda/D + (4 \sin\theta) \cdot \varepsilon \tag{7}$$

Based on Eq. (7), ε can be estimated based on the slope of the $\beta cos\theta$-$4sin\theta$ data. After that, the dislocation density (ρ) can be obtained using the following formula:

$$\rho = 2\sqrt{3} \cdot / (D\,b) \tag{8}$$

The dislocation density of the as-LPBFed samples were calculated to be 1.22×10^{14} m^{-2}, and the increment of YS from dislocation is calculated to be 63.1 MPa.

4.2.3. *Grain boundary strengthening*

The contribution of grain boundary strengthening to yield strength of Al-13.3Mg_2Si alloy can be expressed as Hall–Patch equation shown as [67]:

$$\sigma_{gb} = \sigma_0 + k_y d^{-1/2} \tag{9}$$

where σ_{gb} is the contribution of grain boundary strengthening, σ_0 is the strength of pure aluminium (~20 MPa) [68], k_y is a constant of 0.17 MPa $m^{1/2}$ [68], and d is the mean diameter of grains. The as-LPBFed Al-13.3 Mg_2Si alloy with an average grain size of 18.6 μm. According to Eq. (9), the grain boundary strengthening is estimated as 59.4 MPa.

4.2.4. *Dispersion strengthening*

The dispersion strengthening increment to the yield strength caused by Orowan mechanism is given as [69,70]:

$$\sigma_{dps} = M \frac{0.4Gb}{\pi(1-\nu)^{1/2}} \frac{\ln(2r_m/b)}{\lambda} \tag{10}$$

where Taylor factor (M) is 3.1 [69], shear modulus of the matrix (G) is 26.9 GPa [69], Burger vector (b) is 0.286 nm [71], Poisson's ratio (ν) is 0.33 [71]. r_m is the mean radius of circular cross-section in a random plane for nanoparticles, $r_m = (2/3)^{0.5} r$ [72], where r is the mean radius of the nanoparticles. Meanwhile, λ is the inter-spacing between nanoparticles in the glide plane, which is linked with the diameter r_m and volume fraction f of the nanoparticles, and indicated as [73]:

$$\lambda = 2r_m\left(\sqrt{\frac{\pi}{4f}} - 1\right) \tag{11}$$

Based on SEM and TEM images, the average radius (r) and volume fraction (f) of Mg_2Si nanoparticles are 39.5 nm and 15.7% respectively, which are estimated by Image-Pro Plus. The dispersion strengthening from Mg_2Si nanoparticles contribution to yield strength is estimated to be 252 MPa.

Obviously, the dispersion strengthening (~252 MPa) from Mg_2Si nanoparticles plays a dominant role on the yield strength of the as-LPBFed Al-13.3Mg_2Si alloy. Particularly, several distinctive characteristics of eutectic Mg_2Si are noted in the as-LPBFed alloy, which are the fundamental to differentiate the strength between the Al-13.3Mg_2Si alloy and other reported Al alloys under as-LPBFed condition. (i) The well-developed interface relationship was exsited between the face-cantered cubic Mg_2Si phase and α-Al matrix (Fig. 9f). The fine and divorced eutectic Mg_2Si particles at cell boundaries work as obstacles, which promote Orowan strengthening under loading. (ii) The dispersed eutectic Mg_2Si particles have a higher volume fraction (~15.7%) in this alloy than those of reported as-LPBFed Al–Mg–Si alloys [15–17], resulting in significant enhancement. (iii) The formation of numerous Al–Mg_2Si eutectic benefits to mitigate hot-cracking due to excellent flowability and feeding during eutectic solidification, leading to significant reduction of defects under as-LPBFed condition. Thus, the sacrifice of strength from defects might be restricted to a certain extent. It needs to emphasize that the contributions from α-$Al_{12}(Fe, Mn)_3Si$ phases and GP zone are not taken into account, due to their uneven distribution and low content. It may be resulted that the calculated total yield strength is slightly lower than the actual yield strength measured from experiments.

5. Conclusions

In this study, the pseudo binary eutectic Al-9.6 wt.%Mg-4.9 wt.%Si (Al-13.3 wt.%Mg_2Si) alloy has been successfully processed by LPBF. The process, microstructures and mechanical properties of as-LPBFed alloy were explored. The main conclusions can be summarized as follow:

(1) The high relative density (~99.3%) of the as-LPBFed Al-13.3Mg_2Si alloy was achieved at the VED of 129.6 J/mm^3. Three metallurgical defects were found in the as-LPBFed alloy, including lack of fusion, porosity and keyholes. The excellent processability has been obtained through optimized process parameters and narrow solidification range of 15.3 °C.

(2) The as-LPBFed Al-13.3Mg_2Si alloy were featured by fine α-Al grains and nanosized eutectic Mg_2Si, accompanied by high number density of dislocations, limited coherent GP zone and α-$Al_{12}(Fe,Mn)_3Si$ phases. Typically, the columnar and equiaxed α-Al fine grains were found in the melt pools. The Al–Mg_2Si eutectic microstructures could be divided into three zones, including coarse zone, fine zone and heat affected zone.

(3) The as-LPBFed Al-13.3Mg_2Si alloy exhibited the high ultimate tensile strength of 557 MPa, yield strength of 439 MPa and elongation of 2.9%. The nanoscale eutectic Mg_2Si phases were mainly responsible for the excellent strength. Meanwhile, the rapid solidification from the high cooling rate in LPBF process resulted in the formation of fine α-Al grains, high number density dislocations, supersaturated solid solution, limited GP zone and α-$Al_{12}(Fe,Mn)_3Si$ phases, which are also responsible for strength improvement.

Credit authorship contribution statement

Feipeng Yang: Experiments, data collection and analysis, writing - original draft. **Jianying Wang:** Experiments and data analysis, writing - review. **Tao Wen:** Experiments and data collection. **Xinhai Ai:** Experiments and data analysis. **Xixi Dong:** Conceptualization, writing – review & editing, supervision. **Hailin Yang:** Conceptualization, funding acquisition, project management, supervision, writing - editing & review. **Shouxun Ji:** Conceptualization, results review, writing - editing & review.

Declaration of Competing Interest

The authors declare that they have no known competing financial interests or personal relationships that could have appeared to influence the work reported in this paper.

Acknowledgement

Financial support from the National Key Research and Development Program of China (Grant No. 2020YFB0311300 ZL), and National Natural Science Foundation of China (Grant No. 52071343) are gratefully acknowledged.

REFERENCES

[1] Blakey-Milner B, Gradl P, Snedden G, Brooks M, Pitot J, Lopez E, et al. Metal additive manufacturing in aerospace: a review. Mater Des 2021;209:10008.
[2] Wang YM, Voisin T, McKeown JT, Ye J, Calta NP, Li Z, et al. Additively manufactured hierarchical stainless steels with high strength and ductility. Nat Mater 2018;17(1):63–71.
[3] Zhang D, Qiu D, Gibson MA, Zheng Y, Fraser HL, StJohn DH, et al. Additive manufacturing of ultrafine-grained high-strength titanium alloys. Nature 2019;576(7785):91–5.
[4] Lu W, Zhai W, Wang J, Liu X, Zhou L, Ibrahim AMM, et al. Additive manufacturing of isotropic-grained, high-strength and high-ductility copper alloys. Addit Manuf 2021;38:101751.
[5] Martin JH, Yahata BD, Hundley JM, Mayer JA, Schaedler TA, Pollock TM. 3D printing of high-strength aluminium alloys. Nature 2017;549(7672):365–9.
[6] Aboulkhair NT, Simonelli M, Parry L, Ashcroft I, Tuck C, Hague R. 3D printing of Aluminium alloys: additive Manufacturing of Aluminium alloys using selective laser melting. Prog Mater Sci 2019;106:100578.
[7] Kotadia HR, Gibbons G, Das A, Howes PD. A review of laser powder bed fusion additive manufacturing of aluminium alloys: microstructure and properties. Addit Manuf 2021;46:102155.
[8] Wang Y, Lin X, Kang N, Wang Z, Wang Q, Liu Y, et al. Laser powder bed fusion of Zr-modified Al–Cu–Mg alloy: crack-inhibiting, grain refinement, and mechanical properties. Mater Sci Eng, A 2022;838:142618.
[9] Bi J, Lei Z, Chen Y, Chen X, Lu N, Tian Z, et al. An additively manufactured Al-14.1Mg-0.47Si-0.31Sc-0.17Zr alloy with high specific strength, good thermal stability and excellent corrosion resistance. J Mater Sci Technol 2021;67:23–35.
[10] Zhu Z, Ng FL, Seet HL, Lu W, Liebscher CH, Rao Z, et al. Superior mechanical properties of a selective-laser-melted AlZnMgCuScZr alloy enabled by a tunable hierarchical microstructure and dual-nanoprecipitation. Mater Today 2021;52:90–101.
[11] Zhang J, Gao J, Song B, Zhang L, Han C, Cai C, et al. A novel crack-free Ti-modified Al-Cu-Mg alloy designed for selective laser melting. Addit Manuf 2021;38:101829.
[12] Opprecht M, Garandet JP, Roux G, Flament C, Soulier M. A solution to the hot cracking problem for aluminium alloys manufactured by laser beam melting. Acta Mater 2020;197:40–53.
[13] Li XP, Ji G, Chen Z, Addad A, Wu Y, Wang HW, et al. Selective laser melting of nano-TiB_2 decorated AlSi10Mg alloy with high fracture strength and ductility. Acta Mater 2017;129:183–93.
[14] Zhou SY, Su Y, Wang H, Enz J, Ebel T, Yan M. Selective laser melting additive manufacturing of 7xxx series Al-Zn-Mg-Cu alloy: cracking elimination by co-incorporation of Si and TiB_2. Addit Manuf 2020;36:101458.
[15] Li R, Wang M, Li Z, Cao P, Yuan T, Zhu H. Developing a high-strength Al-Mg-Si-Sc-Zr alloy for selective laser melting: crack-inhibiting and multiple strengthening mechanisms. Acta Mater 2020;193:83–98.
[16] Bi J, Lei Z, Chen Y, Chen X, Tian Z, Liang J, et al. Densification, microstructure and mechanical properties of an Al-14.1Mg-0.47Si-0.31Sc-0.17Zr alloy printed by selective laser melting. Mater Sci Eng, A 2020;774:138931.
[17] Mehta A, Zhou L, Huynh T, Park S, Hyer H, Song S, et al. Additive manufacturing and mechanical properties of the dense and crack free Zr-modified aluminum alloy 6061 fabricated by the laser-powder bed fusion. Addit Manuf 2021;41:101966.
[18] Opprecht M, Garandet J-P, Roux G, Flament C. An understanding of duplex microstructures encountered during high strength aluminium alloy laser beam melting processing. Acta Mater 2021;215:117024.
[19] Wang P, Gammer C, Brenne F, Prashanth KG, Mendes RG, Rümmeli MH, et al. Microstructure and mechanical properties of a heat-treatable Al-3.5Cu-1.5Mg-1Si alloy produced by selective laser melting. Mater Sci Eng, A 2018;711:562–70.
[20] Kimura T, Nakamoto T, Ozaki T, Sugita K, Mizuno M, Araki H. Microstructural formation and characterization mechanisms of selective laser melted Al–Si–Mg alloys with increasing magnesium content. Mater Sci Eng, A 2019;754:786–98.
[21] Kimura T, Nakamoto T, Mizuno M, Araki H. Effect of silicon content on densification, mechanical and thermal properties of Al-xSi binary alloys fabricated using selective laser melting. Mater Sci Eng, A 2017;682:593–602.
[22] Yang F, Wang J, Wen T, Zhang L, Dong X, Qiu D, et al. Developing a novel high-strength Al–Mg–Zn–Si alloy for laser powder bed fusion. Mater Sci Eng, A 2022;851:143636.
[23] Otani Y, Sasaki S. Effects of the addition of silicon to 7075 aluminum alloy on microstructure, mechanical properties, and selective laser melting processability. Mater Sci Eng, A 2020;777:139079.
[24] Montero-Sistiaga ML, Mertens R, Vrancken B, Wang X, Van Hooreweder B, Kruth J-P, et al. Changing the alloy composition of Al7075 for better processability by selective laser melting. J Mater Process Technol 2016;238:437–45.
[25] Zhang H, Wang Y, Wang JJ, Ni DR, Wang D, Xiao BL, et al. Achieving superior mechanical properties of selective laser melted AlSi10Mg via direct aging treatment. J Mater Sci Technol 2022;108:226–35.
[26] Ai X, Wang J, Wen T, Yang F, Dong X, Yang H, et al. A high Fe-containing AlSi12 alloy fabricated by laser powder bed fusion. J Mater Res Technol 2022;18:4513–21.
[27] Wang W, Takata N, Suzuki A, Kobashi M, Kato M. High-temperature strength sustained by nano-sized eutectic

structure of Al–Fe alloy manufactured by laser powder bed fusion. Mater Sci Eng, A 2022;838:142782.
[28] Plotkowski A, Sisco K, Bahl S, Shyam A, Yang Y, Allard L, et al. Microstructure and properties of a high temperature Al–Ce–Mn alloy produced by additive manufacturing. Acta Mater 2020;196:595–608.
[29] Deng J, Chen C, Liu X, Li Y, Zhou K, Guo S. A high-strength heat-resistant Al–5.7Ni eutectic alloy with spherical Al_3Ni nano-particles by selective laser melting. Scripta Mater 2021;203:114034.
[30] Xu JY, Zhang C, Liu LX, Guo R, Sun MJ, Liu L. Achieving high strength in laser powder-bed fusion processed AlFeCuZr alloy via dual-nanoprecipitations and grain boundary segregation. J Mater Sci Technol 2023;137:56–66.
[31] Xu JY, Zhang PC, Guo R, Liu LX, Kang YP, Liu Z, et al. Toughening the additively manufactured Al alloys via manipulating microstructural heterogeneity. J Alloys Compd 2023;945:169322.
[32] Wang L, Qin XY. The effect of mechanical milling on the formation of nanocrystalline Mg_2Si through solid-state reaction. Scripta Mater 2003;49:243–8.
[33] Li SP, Zhao SX, Pan MX, Zhao DQ, Chen XC, Barabash OM, et al. Solidification and structural characteristics of α-(Al)-Mg_2Si eutectic. Mater Trans 1997;38(6):553–9.
[34] Zhu X, Yang H, Dong X, Ji S. The effects of varying Mg and Si levels on the microstructural inhomogeneity and eutectic Mg_2Si morphology in die-cast Al–Mg–Si alloys. J Mater Sci 2018;54(7):5773–87.
[35] Ji S, Yan F, Fan Z. Development of a high strength Al–Mg_2Si–Mg–Zn based alloy for high pressure die casting. Mater Sci Eng, A 2015;626:165–74.
[36] Yang H, Zhang YY, Wang JY, Liu ZL, Liu XC, Ji SX. Additive manufacturing of a high strength Al-5Mg_2Si-2Mg alloy: microstructure and mechanical properties. J Mater Sci Technol 2021;91:215–23.
[37] Prashanth KG, Scudino S, Maity T, Das J, Eckert J. Is the energy density a reliable parameter for materials synthesis by selective laser melting? Mater Res Lett 2017;5(6):386–90.
[38] Liu X, Zhao C, Zhou X, Shen Z, Liu W. Microstructure of selective laser melted AlSi10Mg alloy. Mater Des 2017;168:107677.
[39] Wang X, Ma PK, Zhang SY, Liu X, Wang C, Wang DW, et al. High-ductility AA6061 alloys produced by combination of sub-rapid solidification and Cr-alloying. J Mater Res Technol 2022;18:1566–77.
[40] Geng R, Qiu F, Zhao QL, Gao YY, Jiang QC. Effects of nanosized TiCp on the microstructure evolution and tensile properties of an Al-Mg-Si alloy during cold rolling. Mater Sci Eng, A 2019;743:98–105.
[41] Yin HS, Song M, Deng P, Li L, Prorok BC, Lou XY. Thermal stability and microstructural evolution of additively manufactured 316L stainless steel by laser powder bed fusion at 500–800 °C. Addit Manuf 2021;41:101981.
[42] Guo Y, Jia L, He J, Zhang S, Li Z, Zhang H. Interplay between eutectic and dendritic growths dominated by Si content for Nb-Si-Ti Alloys via rapid solidification. J Manuf Sci Eng 2022;144(6):061007.
[43] Czerwinski F. The growth of quaternary divorced eutectic in Al–Ce–Si–Mg alloys. Metall Mater Trans A 2022;54(2):391–8.
[44] Shimosaka D, Kumai S, Casarotto F, Watanabe S. Effect of cooling rates during Solidification of Al-5.5%Mg-2.3%Si-0.6%Mn and Al-13%Mg_2Si pseudo-binary alloys on their secondary-particle morphology and tear toughness. Mater Trans 2011;52(5):920–7.
[45] Hyer H, Zhou L, Mehta A, Park S, Huynh T, Song S, et al. Composition-dependent solidification cracking of aluminum-silicon alloys during laser powder bed fusion. Acta Mater 2021;208:116698.
[46] Chen B, Moon SK, Yao X, Bi G, Shen J, Umeda J, et al. Strength and strain hardening of a selective laser melted AlSi10Mg alloy. Scripta Mater 2017;1410:45–9.
[47] Rao JH, Zhang Y, Fang X, Chen Y, Wu X, Davies CHJ. The origins for tensile properties of selective laser melted aluminium alloy A357. Addit Manuf 2017;17:113–22.
[48] Wang M, Song B, Wei Q, Zhang Y, Shi Y. Effects of annealing on the microstructure and mechanical properties of selective laser melted AlSi7Mg alloy. Mater Sci Eng, A 2019;739:463–72.
[49] Rashid R, Masood SH, Ruan D, Palanisamy S, Rahman Rashid RA, Elambasseril J, et al. Effect of energy per layer on the anisotropy of selective laser melted AlSi12 aluminium alloy. Addit Manuf 2018;22:426–39.
[50] Wang XJ, Zhang LC, Fang MH, Sercombe TB. The effect of atmosphere on the structure and properties of a selective laser melted Al–12Si alloy. Mater Sci Eng, A 2014;597:370–5.
[51] Suryawanshi J, Prashanth KG, Scudino S, Eckert J, Prakash O, Ramamurty U. Simultaneous enhancements of strength and toughness in an Al-12Si alloy synthesized using selective laser melting. Acta Mater 2016;115:285–94.
[52] Li W, Li S, Liu J, Zhang A, Zhou Y, Wei Q, et al. Effect of heat treatment on AlSi10Mg alloy fabricated by selective laser melting: microstructure evolution, mechanical properties and fracture mechanism. Mater Sci Eng, A 2016;663:116–25.
[53] Aboulkhair NT, Maskery I, Tuck C, Ashcroft I, Everitt NM. The microstructure and mechanical properties of selectively laser melted AlSi10Mg: the effect of a conventional T6-like heat treatment. Mater Sci Eng, A 2016;667:139–46.
[54] Uddin SZ, Murr LE, Terrazas CA, Morton P, Roberson DA, Wicker RB. Processing and characterization of crack-free aluminum 6061 using high-temperature heating in laser powder bed fusion additive manufacturing. Addit Manuf 2018;22:405–15.
[55] Biswas P, Mandal D, Mondal MK. Failures analysis of in-situ Al–Mg_2Si composites using actual microstructure based model. Mater Sci Eng, A 2020;797:140155.
[56] Favaloro T, Bahk JH, Shakouri A. Characterization of the temperature dependence of the thermoreflectance coefficient for conductive thin films. Rev Sci Instrum 2015;86(2):024903.
[57] Li Y, Gu D. Parametric analysis of thermal behavior during selective laser melting additive manufacturing of aluminum alloy powder. Mater Des 2014;63:856–67.
[58] DebRoy T, Wei HL, Zuback JS, Mukherjee T, Elmer JW, Milewski JO, et al. Additive manufacturing of metallic components – process, structure and properties. Prog Mater Sci 2018;92:112–224.
[59] Ali H, Ma L, Ghadbeigi H, Mumtaz K. In-situ residual stress reduction, martensitic decomposition and mechanical properties enhancement through high temperature powder bed pre-heating of selective laser melted Ti6Al4V. Mater Sci Eng, A 2017;695:211–20.
[60] Kou S. A criterion for cracking during solidification. Acta Mater 2015;88:366–74.
[61] Tan Q, Fan Z, Tang X, Yin Y, Li G, Huang D, et al. A novel strategy to additively manufacture 7075 aluminium alloy with selective laser melting. Mater Sci Eng, A 2021;821:141638.
[62] Kingery WD. Factor affecting thermal stress resistance of ceramic materials. J Am Ceram 1955;38:3–15.
[63] Hanemann T, Carter LN, Habschied M, Adkins NJ, Attallah MM, Heilmaier M. In-situ alloying of AlSi10Mg+ Si using Selective Laser Melting to control the coefficient of thermal expansion. J Alloys Compd 2019;795:8–18.
[64] Yuan SP, Liu G, Wang RH, Pu X, Zhang GJ, Sun J, et al. Coupling effect of multiple precipitates on the ductile fracture of aged Al–Mg–Si alloys. Scripta Mater 2007;57(9):865–8.
[65] Myhr OR, Grong Ø, Andersen SJ. Modelling of the age hardening behaviour of Al–Mg–Si alloys. Acta Mater 2001;49:65–75.

[66] He JY, Wang H, Huang HL, Xu XD, Chen MW, Wu Y, et al. A precipitation-hardened high-entropy alloy with outstanding tensile properties. Acta Mater 2016;102:187–96.
[67] Wang Y, Deng YL, Dai QS, Jiang K, Guo X. Microstructures and strengthening mechanisms of high Fe containing Al–Mg–Si–Mn–Fe alloys with Mg, Si and Mn modified. Mater Sci Eng, A 2021;803:140477.
[68] Jia Q, Rometsch P, Kürnsteiner P, Chao Q, Huang A, Weyland M, et al. Selective laser melting of a high strength Al-Mn-Sc alloy: alloy design and strengthening mechanisms. Acta Mater 2019;171:108–18.
[69] Ma K, Wen H, Hu T, Topping TD, Isheim D, Seidman DN, et al. Mechanical behaviour and strengthening mechanisms in ultrafine-grain precipitation-strengthened aluminum alloy. Acta Mater 2014;62:141–55.
[70] Xiong T, Zheng SJ, Pang JY, Ma XL. High-strength and high-ductility AlCoCrFeNi2.1 eutectic high-entropy alloy achieved via precipitation strengthening in a heterogeneous structure. Scripta Mater 2020;186:336–40.
[71] Hu ZH, Zhang H, Zhu HH, Xiao ZX, Nie XJ, Zeng XY. Microstructure, mechanical properties and strengthening mechanisms of AlCu5MnCdVA aluminum alloy fabricated by selective laser melting. Mater Sci Eng, A 2019;759:154–66.
[72] Hirsch PB, Humphreys FJ. The physics and strength of plasticit. MIT Press Cambridge; 1969.
[73] Brown RHL. Strengthening methods in crystals. Elsevier Amsterdam; 1971.